General Synthesis of Ultrafine Metal Oxide/Reduced Graphene Oxide Nanocomposites for Ultrahigh-Flux Nanofiltration Membrane

Wanyu Zhang
  East China University of Science and Technology
Hai Xu
  East China University of Science and Technology
Fei Xie
  East China University of Science and Technology
Xiaohua Ma
  East China University of Science and Technology   https://orcid.org/0000-0002-3902-1808
Bo Niu
  East China University of Science and Technology
Mingqi Chen
  East China University of Science and Technology
Hongyu Zhang
  East China University of Science and Technology
Yayun Zhang
  East China University of Science and Technology
Donghui Long (✉ longdh@mail.ecust.edu.cn)
  East China University of Science and Technology   https://orcid.org/0000-0002-3179-4822

Abstract

Graphene-based membranes have great potential to revolutionize nanofiltration technology, but achieving high solute rejections at high water flux remains extremely challenging. Herein, a family of ultrafine metal oxide/reduced graphene oxide (rGO) nanocomposites are synthesized through a heterogenous nucleation and diffusion-controlled growth process for dye nanofiltration. The synthesis is based on the utilization of oxygen functional groups on GO surface as preferential active sites for heterogeneous nucleation, leading to the formation of sub-3nm size, monodispersing as well as high-density loading of metal oxide nanoparticles. The anchored ultrafine nanoparticles could inhibit the wrinkling of the rGO nanosheet, forming highly stable colloidal solutions for solution-processing fabrication of nanofiltration membranes. By functioning as pillars, the nanoparticles remarkably increase both vertical interlayer spacing and lateral tortuous paths of the rGO membranes, offering an unprecedented water permeability of 225 L m^{-2} h^{-1} bar^{-1} and a high selectivity up to 98% in the size-exclusion separation of methyl blue.

Introduction

Nanofiltration is an energy-efficient membrane separation process that can reject efficiently multivalent ions and organic compounds, showing great promising in water treatment applications, and particularly in pharmaceutical and food industries[1–4]. Generally, the nanofiltration membranes have nanopores in the range of 0.5-5 nm which could fulfill nominal molecular weight cut-off of 200–1000 Da[5, 6]. And the separation mechanism is majorly governed by the size-based and charge-based exclusion which depends strongly both on the membrane structure and on the interaction between the membrane and the solute[7, 8].

Recently, a great advance has been made in the graphene-based membranes for nanofiltration[9]. Graphene is an up-and-coming 2D material with good flexibility, large surface area, excellent electrical conductivity and high surface activity[10]. It thus has been considered as an ideal membrane material especially for desalination[11]. More typically, the graphene oxide (GO) composed of graphite-like and oxidized region feature water migration and simultaneously highly efficient molecule sieving[12]. GO is dispersible in water and many other polar solvents, making it be easily fabricated into laminated membrane materials via solution processing techniques for nanofiltration separations[13–18]. The 2D interlayer spacing between GO nanosheets can be used as nanochannels for water permeation while rejecting the larger species[19]. And the interlayer spacing of GO nanosheets can be further adjusted to achieve size-selective molecular sieving[20]. However, GO nanosheets are extremely hydrophilic, causing uncontrollable swelling and poor stability of GO membranes in water environments[21, 22]. Therefore, the reduced graphene oxide (rGO) membranes with lower oxygen functional groups can provide better performances in precise molecular sieving, due to their narrower nanochannels, lower swelling and higher stable in water or harsh chemical conditions[23, 24]. Unfortunately, water permeation through the stacked GO or rGO membranes is insufficient due to the strong capillary force and the narrow nanochannels[25].

Broadening the interlayer spacings have been employed to modulate the water transport behaviors in GO membranes, generally via intercalation of soft polymers including cationic porphyrin[26], polyacrylonitrile gel[27], polyelectrolyte brushes[28]. However, incorporating polymer additives often cause very limited enhancement of water permeability, mainly owing to the intrinsic elastoplastic of the polymers and their uneven distribution on the GO surface[29, 30]. In addition, the enlarged interlayer spacing will make a trade-off between permeability and selectivity, inducing significant rejection degradation[31, 32]. It should be beneficial for tailoring the interlayer distance and improving membrane permeability if the intercalation materials is rigid and highly dispersed, but a practical intercalation strategy has remained elusive.

Herein, we report a general and facile colloidal synthesis to prepare ultrafine metal oxide/rGO nanocomposites for nanofiltration membranes. The synthesis is based on the utilization of oxygen functional groups on GO surface as preferential sites for fast heterogeneous nucleation, leading to the formation of sub-3 nm size, monodispersing as well as high-density loading of metal oxide nanoparticles on the rGO surface. The present synthesis is highly universal for anchoring various metal oxide nanoparticles, such as ZnO, CoO, CuO, MgO, Fe_2O_3, Nb_2O_5, CdO, La_2O_3, and MoO_3 and metal sulfides such as ZnS, MoS_2 nanoparticles. Moreover, adhesion of these ultrafine nanoparticles could inhibit the wrinkling and restacking of the rGO nanosheet, forming highly stable colloidal solutions for low-cost solution processing of nanofiltration membranes. By functioning as rigid pillars, the nanoparticles not only increase the distance between the rGO sheets, but also create narrow tortuous paths among the 2D nanochannels for size-exclusion separation of dye molecules. The resulting membranes could realize unprecedented water permeability (225 L m^{-2} h^{-1} bar^{-1}) and high selectivity (up to 98%) of methyl blue, which places them among the most effective dye separation membranes reported to date. This study illustrates the utility of rigid nanoparticles as spacers for addressing the permeability-selectivity trade-off of GO-based membranes, providing insights into the design of next-generation nanofiltration membranes.

Results

Synthesis and characterization of ultrafine ZnO/rGO nanocomposites.
Figure 1a illustrates a general heterogeneous nucleation and diffusion-controlled growth process of ultrafine metal oxide/rGO nanocomposites using ultrafine ZnO/rGO nanocomposites as an example. The GO is rich in oxygen functional groups, and it is supposed that these oxygen functional groups are responsible for the heterogeneous nucleation. More typically, in a mixed ethylene glycol (EG) solution of GO and zinc acetate dihydrates (Zn(Ac)$_2$·2H$_2$O), the presence of oxygen groups which contributes to an overall negatively charged surface of -40 mV will capture the positively charged [Zn(EG)$_2$]$^{2+}$ complexes through electrostatics interactions (**Fig. S1**). Under solvothermal conditions, the adsorbed [Zn(EG)$_2$]$^{2+}$ complexes could be hydrolyzed to adsorbed Zn(OH)$_2$, which is equivalent to the formation of preferential sites. At such sites, the effective surface energy is lower, thus diminishes the free energy barrier and facilitating heterogeneous nucleation. The as-formed nucleus will grow slowly via a diffusion-controlled growth process, leading to the formation of ultrafine and isolated island nanoparticles on the surface of rGO.

The TEM images reveal that the as-prepared ZnO/rGO nanocomposites has a very transparent laminated structure with less wrinkles and folding, which is similar to the pristine GO nanosheets (Fig. 1b). The high-resolution TEM images (Fig. 1c-d) clearly demonstrate that the rGO surface is consisted of densely distributed ZnO nanoparticles with the size of ca. 2.5 nm. Besides, energy dispersive X-ray spectroscopy (EDS) elemental mappings (Fig. 1e) also confirm that ZnO nanoparticles are distributed homogeneously within the rGO nanosheets. The weight ratio of ZnO in the composite is determined to be close to the designed value 50 wt% (Fig. 2f), suggesting that all Zn precursors participate fully the hydrolysis reaction to ZnO.

Mechanism study of the formation of ultrafine ZnO nanoparticles on GO surface. To understand the nucleation and growth of ZnO nanoparticles on rGO surface, the time-dependent experiments were conducted. At the initial solvothermal time of 0.5 h, the ZnO nanoparticles are already formed, but their size is only 1 nm corresponding to ~ 20 ZnO molecular clusters (Fig. 2a and **Fig. S2**). With the time prolonging, the size gradually increases to ca. 2.5 nm at 3 h while remains unchanged until reaching to their final stage (Fig. 2b-e). It is interesting to note that the particle number density is almost the same of 9 per 10 nm·10 nm for all samples (Fig. 2e and **Fig. S3**), which clearly indicates that the nucleation occurs simultaneously at GO surface and no new nuclei form during growth process. This result implies that the particle number density should be depended on the surface characteristics of GO, more especially the number of oxygen functional groups.

To verify the structure and chemical state of the nanocomposites produced at the first few hours of solvothermal synthesis, the thermogravimetric (TG), X-ray photoelectron (XPS), and X-ray diffraction (XRD) characterizations were conducted. The weight ratio of ZnO in composites from TG results (Fig. 2f) has similar increasing tendency with the size of ZnO nanoparticles. At the initial 0.5 h, the weight ratio of ZnO nanoclusters is only 10 wt%, and then gradually increases to the designed value of 50 wt% at 3 h. It is noted that the ZnO/rGO-0.5 h has a significant weight loss at temperature of 160–220 °C in TG curve, which should be due to deoxygenation of incompletely reduced GO. This could be well confirmed by XRD pattern (Fig. 2g), in which the ZnO/rGO-0.5 h exhibit two shoulder peaks centered at 11° and 23°, responding to the characteristic of GO and rGO[33, 34], respectively. While the time increase to 2 h, the characteristic peak at 10° disappears, suggesting the successful reduction of GO. And no obvious characteristic peaks could be discerned for the ZnO crystals, further confirming their ultrafine size. In addition, XPS patterns (Fig. 2h-i and **Fig. S4**) suggest that the GO is incompletely reduced at the initial 0.5 h, as indicated by a high ratio of C = O. It should be noted that the Zn 2p spectra (Fig. 2j) for all samples are very similar with two obvious bands located at 1045.3 eV and 1022.3 eV, corresponding to the Zn^{2+} $2p_{1/2}$ and Zn^{2+} $2p_{3/2}$, respectively[35]. All these results indicates that the reduction of GO and the growth of ZnO on rGO nanosheets could be accomplished at the initial 3 h under solvothermal conditions.

The key to the synthesis of ultrafine ZnO nanoparticles should be the oxygen functional groups on GO surface, which have binding ability toward Zn^{2+} through electrostatic attractions, and consequently trigger the heterogenous nucleation. According to the elemental analysis, GO used in this work has a C/O

ratio of ca.1.8. And XPS spectrum in Fig. 2h reveals that it is consisted of majorly epoxide and carbonyl functional groups on the basal plane, and hydroxyl and carboxyl groups on its edges[36]. To get insights into the binding abilities of these oxygen functional groups with Zn $^{2+}$ in EG, we perform density-functional theory (DFT) calculation and disclose that the order of adsorption stability towards Zn^{2+} is as follows: epoxy(-COC) > carbonyl (-CO) > carboxyl (-COOH) > > hydroxyl (-OH) (Fig. 3a). Furthermore, the hydrolysis of adsorbed Zn^{2+} and then its transformation to ZnO on GO surface and without GO are analyzed. The optimized structures of intermediates and their Gibbs free profiles are displayed in Fig. 3b-c and **Table S1**. The overall Gibbs free energy changes on oxygen functional groups (-OH, -COC, -COOH and -CO) in EG reaction system are − 6.433 eV, -6.999 eV, -6.608 eV, and − 7.759 eV, respectively, which are all more negative than that of without GO (-4.783 eV). The last step of Zn(OH)$_2$/rGO*→ZnO/rGO* exhibits positive Gibbs energy change (ΔG), which infers this step is the thermodynamic-limiting step in the whole process. From the results of Gibbs energy changes, it can be concluded that the total transformation process of Zn^{2+} to ZnO is a spontaneous process and thermodynamically more favorable on GO surface. The carbonyl is suggested as the most active site for nucleation and followed by epoxy and carboxyl.

The controlled nucleation is triggered by the oxygen functional groups on GO surface due to the lower free energy barrier, while the consequent growth of ZnO nanoparticles should be a diffusion-controlled process that is limited by the rate of incorporation of adatoms into ZnO growth centers. Herein, the growth of ZnO nanoparticles on the rGO surface was studied through a series of control experiment by changing the reaction temperature. As shown in **Fig. S5a**, the ZnO/rGO nanocomposites prepared at temperature of 90°C show ultrasmall ZnO nanoparticles of ca. 1.3 nm. Such low nucleation temperature should be due to the lowering heterogenous nucleation barrier, while the small size should be caused by the limited diffusion at low temperature. With increasing the reaction temperature to 180°C, the average size of ZnO nanoparticle increases gradually, but the particle number density keeps almost unchanged on the rGO surface (**Fig. S5-7**). In addition, the concentration of precursor Zn (Ac)$_2$·2H$_2$O was also changed to adjust the loading contents of ZnO in ZnO/rGO nanocomposites. At a low precursor concentration, the TG curve reveals that the content of ZnO is 30 wt%, being the same with the designed value (**Fig. S7b**). However, the resulting nanocomposites (**Fig. S5d**) show an almost transparent feature without the visible nanoparticles on the rGO surface, which should be due to the formation of ultrasmall ZnO clusters (< 1 nm) that are hardly displayed by the TEM images. While the ZnO loading is larger than 50%, the nanocomposites show almost similar morphologies of ZnO nanoparticles (**Fig. S5e-f** and **Fig. S7b**).

Furthermore, the synthesis of pure ZnO particles without GO was conducted under the same solvothermal conditions. The obtained ZnO product shows spherical aggregates with size of ca. 600 nm (**Fig. S8**), which should be due to the homogenous nucleation continued by the growth of primary nanoparticles and thereafter the spherical aggregation. In addition, the solvent is also critical for the formation uniform ZnO nanoparticles on the rGO surface. EG is selected as the solvent due to its strong chelating and reduction ability[37]. While changing solvent from EG to deionized water and ethanol (**Fig. S9-10**), large and aggregated particles are formed on the wrinkled rGO surface.

General synthesis of ultrafine metal oxide/rGO nanocomposites. Based on the above discussion, the oxygen functional groups-induced heterogenous nucleation should work as a general strategy for the synthesis of other metal oxide/rGO nanocomposites. Herein, a family of nanocomposites with ultrafine metal oxide nanoparticles grown on rGO surface are successfully prepared, including CdO/rGO, CoO/rGO, CuO/rGO, Fe_2O_3/rGO, MgO/rGO, La_2O_3/rGO, MoO_3/rGO and Nb_2O_5/rGO. As shown in **Fig.4a-h** and **Fig. S11-12**, TEM images verify that all nanocomposites consist of monodispersed ultrafine metal oxide nanoparticles with the size less than 3 nm. Moreover, metal sulfide nanoparticles/rGO nanocomposites, such as ZnS/rGO and MoS_2/rGO could also be prepared by the present strategy through adding the thiourea in the precursor solution, as shown in **Fig. 4i-j** and **Fig. S13**.

The synthetic procedures reported in this work is highly reproducible and readily applicable for the large-scale synthesis of ultrafine metal oxide/rGO nanocomposites. And more importantly, due to the effective inhibition of wrinkling of the rGO sheets, the as-prepared nanocomposites are highly dispersed into EG, forming a homogenous colloidal suspension of ca. 4 mg/ml without obvious sedimentation even after one month (**Fig. 4k**). Furthermore, the as-prepared nanocomposites could be also dispersed in the organic solvent such as N, N-dimethylformamide (DMF), isopropanol or N-methylpyrrolidone (NMP), which are desirable for wet processing to enable a homogenous arrangement of nanocomposites as filler, coatings, or thin films.

Preparation and characterization of ZnO/rGO membranes. The free-standing ZnO/rGO nanocomposite membranes were fabricated by a simple vacuum filtration of homogenous colloidal suspensions. The continuous suction force from vacuum pump can move the solvent rapidly, which could overcome the agglomeration of nanocomposites and form the laminated membranes. After being washed with ethanol and dried in 60°C, the ZnO/rGO membrane with 45 mm diameter is obtained (Fig. 5a). This membrane can randomly bend 360°, suggesting its excellent flexibility and durability. SEM images (Fig. 5b) indicates that the resulting membrane is continuous and free of macropores or surface defects. And the cross-section image (Fig. 5c) demonstrates a layered structure resembling that of nacre, therefore exhibiting good mechanical strength. The distance between ZnO/rGO bilayer is ~ 4.6 nm determined by AFM images (Fig. 5d-e). By subtracting the rGO monolayer (ca. 0.34–0.4 nm)[23], the 2D nanochannel spacing of ZnO/rGO membrane is estimated at ~ 4.2 nm. Furthermore, the interlayer spacings between nanosheets as pores are evaluated by nitrogen adsorption-desorption measurement. As shown in Fig. 5f, ZnO/rGO membrane displays a Type IV sorption isotherm with Type H3 hysteresis[38], responding to the slit-shaped pores between nanosheets. The resulting BJH pore size distribution reveals that the average pore size is at ~ 4.0 nm, which is consistent with AFM results.

Nanofiltration performance of ZnO/rGO membranes. GO-based membranes are great promising for advanced nanofiltration in water treatments, however their narrow interlayer channels generally limit the water flux and the separation of larger organic molecules[39]. Generally, the separation mechanism of GO-membranes is governed primarily by the interlayer spacing between the nanosheets and the length or tortuosity of the transport pathways[40]. By functioning as pillars, the metal oxide nanoparticles remarkably increase both vertical interlayer spacing and lateral tortuous paths of the rGO membranes,

offering the great possibility for the membranes concurrently with high water permeance and high rejections (as illustrated in Fig. 6a).

To evaluate the separation performance, we fabricated the ZnO/rGO membranes supported by nylon substrates and used them for dye permeation tests. As shown in **Fig. S16**, ZnO/rGO membranes are uniformly coated on a porous nylon 66-0.22 μm substrate. The surface wettability of ZnO/rGO membranes is determined to be ca. 46° by the water contact angle (**Fig. S17**), indicating excellent hydrophilic properties. The loading mass of ZnO/rGO on nylon membranes can be changed from 0.14 to 0.58 mg cm^{-2} by varying the volume of colloidal dispersion during the vacuum filtration. The average thicknesses of the ZnO/rGO membranes are in the range of nanometers (220 nm) to micrometers (1.1 μm) estimated by the SEM observation (**Fig. S18**).

Due to the variations in transport distance, the loading mass of nanosheets has a critical effect on the water flux and the rejection rate of methyl blue (MB), as shown in Fig. 6b. With the increase of the ZnO/rGO loading mass, the rejection rate increase from 69−98.1%, while water flux decreases from 390 to 190 L m^{-2} h^{-1} bar^{-1}. Therefore, we select the optimized loading mass of ca. 0.54 mg cm^{-2} for further performance evaluation, which achieve simultaneously an extraordinary high-water flux of 225 L m^{-2} h^{-1} bar^{-1} and MB rejection of 98.1 %. To highlight the advanced performance of ZnO/rGO membranes, the pure GO membranes at the same mass loadings are prepared, which exhibits only 20 L m^{-2} h^{-1} bar^{-1} water permeance as given in Fig. 6c. Moreover, the MB rejections of other reported GO-based membranes are compared in Fig. 6d and **Table S2**. Except the exciting rejection rate, the ZnO/rGO membranes exhibit much higher water permeance than those of the GO-based membranes reported so far (generally less than 80 L m^{-2} h^{-1} bar^{-1}) [41−51].

Molecular selectivity is one of crucial parameters for the nanofiltration. Here we select a series of dye molecules with different molecular weights (361 ~ 960 Da, including evans blue (EB), congo red (CR) and chrome black T (CBT), methyl orange (MO)) for the comparison, and their chemical structures and molecular sizes are given in **Table S3**. Although the interspacing of ZnO/rGO layers (~ 4.2 nm) is much larger than the molecular sizes of these dyes, the ZnO/rGO membranes still exhibit remarkably high rejections of > 95% for EB, CR and CBT at high water permeances of ~ 220 L m^{-2} h^{-1} bar^{-1}, as shown in Fig. 6e. Such excellent rejections should be due to the additional blocking and sieving effects by these monodispersed ZnO nanoparticles, which create narrow and tortuous paths in the 2D interlayer spaces. However, in the case of MO with smallest molecular size of 1.13 nm × 0.42 nm, the ZnO/rGO membranes show only 27% rejection as a result of ineffective sieving effects for smaller molecules.

The long-term stability of ZnO/rGO and GO membranes were also conducted over a duration of 30 h. As shown in Fig. 6f, the GO membranes deliver an initial water flux of 20 L m^{-2} h^{-1} bar^{-1} and then decline rapidly to 3 L m^{-2} h^{-1} bar^{-1}, due to the compression of loosely overlapped GO nanosheets under pressure. On the contrast, the rigid ZnO nanoparticles could serve as rigid "pillars" to create permanent

high-speed waterways along the surface of rGO nanosheets, achieving a high steady-state flux value of 160 L m^{-2} h^{-1} bar^{-1} after steadily 30 h working.

Discussion

The separation mechanism of ZnO/rGO membranes for dye molecules should be dominated by size-exclusion selectivity, based on the counteracting roles of enlarging interlayer spacing and in-plane steric effects both caused by high-density loading of ultrafine ZnO nanoparticles. Water molecules could easily pass through the spaces between the pillars, while large-molecular dyes are selectively blocked based on their size and shape. The ZnO/rGO membranes thus address the critical trade-off between water flux and dye rejection in contrast to conventional nanofiltration membranes. Furthermore, the membrane microstructure could be adjusted by using different nanoparticle sizes and loadings, allowing us to control both the height and width of the paths between the pillars, thereby offering the great possibility towards on-demand nanofiltration applications.

In conclusion, we demonstrate a general and facile method to synthesize ultrafine metal oxide/rGO nanocomposites through heterogenous nucleation and growth process for nanofiltration applications. The key to the present synthesis is employing the oxygen functional groups on GO, which have binding ability toward Zn^{2+} through electrostatic attractions, and sequently triggers the heterogenous nucleation. Another important merit of the present synthesis is the effective inhibition of wrinkling and stacking of the resulting rGO sheets via the uniform adhesion of these ultrafine metal oxide nanoparticles. The adhesion of these metal oxide nanoparticles not only leads to physical separation of the rGO sheets, but also forms stable dispersions for wet processing of the membranes. Water molecules could easily pass through the narrow spaces between the nanoparticles, while large-molecular dyes are selectively rejected based on their size and shape. Moreover, the membrane microstructure can be turned vertically and laterally by using different sizes and loadings of metal oxide nanoparticles, extending their great potentials for on-demands applications such as water treatment, solvent dehydration, and organics sieving.

Methods

Synthesis of ultrafine ZnO/rGO nanocomposites. Graphene oxide (GO) was prepared by a modified Hummers method[52]. The as-prepared GO nanosheets were dispersed into EG to form a homogenous solution of 5 mg/ml. And 0.27 g zinc acetate dihydrate ($Zn(Ac)_2 \cdot 2H_2O$) was dissolved in a 30 mL EG with ultrasound for 1 h to form a transparent solution. Then, $Zn(Ac)_2 \cdot 2H_2O$/EG solution was added to 25 mL GO/EG solution. After continuous magnetic stirring for about 2 h, the resultant solution 55 mL Zn (Ac)$_2$-GO/EG solution was transferred into a 100 mL Teflon-lined stainless-steel autoclave and heated at 180 °C for 24 h. After cooling down to room temperature naturally, the ultrafine ZnO/rGO nanocomposites were obtained. The designed ZnO content in the composite is 50%.

In a control experiment, the solvothermal time was changed to 0.5 h, 1 h, 2 h, 3 h, 8 h, and 12 h, ZnO/rGO-1 h, ZnO/rGO-2 h, ZnO/rGO-3 h, ZnO/rGO-8 h, and ZnO/rGO-12 h were obtained, respectively. The samples prepared at different temperature of 90 °C, 120 °C, and 150 °C were denoted as ZnO/rGO-90°C, ZnO/rGO-120°C, and ZnO/rGO-150°C, respectively. The samples prepared with different $Zn(Ac)_2 \cdot 2H_2O$ weight of 0.12 g and 0.63 g were denoted as ZnO/rGO-30% and ZnO/rGO-70%, respectively. The samples synthesized in different solvent of deionized water and ethanol were denoted as $ZnO/rGO-H_2O$ and ZnO/rGO-EtOH. Pure ZnO was synthesized without adding GO/EG suspension in preparation.

Synthesis of other ultrafine metal oxide/rGO nanocomposites. All ultrafine metal oxide/rGO nanocomposites (CdO/rGO, CoO/rGO, CuO/rGO, Fe_2O_3/rGO, MgO/rGO, La_2O_3/rGO, MoO_3/rGO, and Nb_2O_5/rGO) were synthesized using the same process as that of ultrafine ZnO/rGO nanocomposites, except that $Zn(Ac)_2 \cdot 2H_2O$ was replaced by other metal salts ($Cd(Ac)_2 \cdot 2H_2O$, $Co(Ac)_2 \cdot 4H_2O$, $Cu(Ac)_2 \cdot H_2O$, $Fe(Ac)_2 \cdot 4H_2O$, $Mg(Ac)_2$, $La(Ac)_3 \cdot 6H_2O$, $Mo_7O_{24}(NH_4)_6 \cdot 4H_2O$, and $NbCl_5$). The designed contents of all metal oxide in nanocomposites are 50%.

Synthesis of ultrafine metal sulfide/rGO nanocomposites. The ultrafine ZnS/rGO and MoS_2/rGO nanocomposites were prepared by the same way of ZnO/rGO and MoO_3/rGO nanocomposites, respectively, through adding the thiourea in the precursor solution. The designed contents of all metal sulfide in nanocomposites are 50%.

Preparation of ZnO/rGO free-standing membranes. A certain amount of ultrafine ZnO/rGO nanocomposites were dispersed into EG to form a homogenous solution. And then the solution was vacuum filtered with polyvinylidene difluoride (PVDF) membranes. The wet ZnO/rGO nanocomposites with PVDF membranes were fabricated and washed with ethanol several times. After being dried in 60°C for 12 h, the ZnO/rGO membranes could be peeled off as a free-standing membrane.

Materials characterizations. The morphologies and structures of nanocomposites were observed by using transmission electron microscopy (TEM, JEM-2100), scanning electron microscopy (SEM, Nova NanoSEM 450), and atomic force microscopy (AFM, MFP-3D). The thermogravimetric analysis (TGA 8000) was carried out at an air flow of 30 mL min^{-1} with heating from 30 °C to 800 °C at a rate of 10 °C min^{-1}. The X-ray diffraction (XRD) patterns were obtained by using Cu Kα radiation (λ = 1.5406 Å) on a Rigaku D/Mac 2550 diffractometer. The X-ray photoelectron spectroscopy (XPS) were carried out using ESCALAB 250Xi. Zeta potential pattern was obtained by using a Zetasizernano. The elemental composition was obtained from the CHN elemental analysis (Elementar Vario EL; Thermo Fisher). The N2 adsorption-desorption isotherm was carried out by ASAP2460, while the pore size was determined by Barrett−Joyner−Halenda (BJH) theory.

Density Functional Theory calculations. All the calculations were carried out by using the Perdew-Burke-Ernzerhof (PBE) function based on density functional theory (DFT) within the Vienna Ab Initio Simulation Package (VASP). To describe the electron − ion interactions, the cutoff energy of the plane wave was set as 400 eV. All atomic structures were allowed to relax until the maximum force was smaller than 0.02 eV/

Å with the energy convergence criterion of 10^{-5} eV. And the 25 Å was set as the thickness of vacuum layer to avoid periodic effects between mirror images. The graphene sheets containing defects were simulated by the 8·8·1 supercells of repeated model. Integration of the Brillouin zone was performed by 1·1·1 k-point grids based on Gamma Scheme to obtain the optimized configuration and total energy of the system. What's more, Bader charge difference analysis was adopted to describe the charge transfer within the system.

The adsorption energy (E_{ads}) was calculated according to the following equation:

$E_{ads} = E_{adsorbate,sub} - E_{sub} - E_{adsorbate}$ (1)

Where $E_{adsorbate, sub}$ represents the total energy of the adsorbate on the substrate, E_{sub} represents the energy of the adsorbate, and $E_{adsorbate}$ represents the energy of the adsorbate.

The Gibbs free-energy difference (ΔG) of reaction pathways was calculated according to the following equation:

$\Delta G = \Delta H + \Delta E_{zpe} - T\Delta S$ (2)

Where ΔH, ΔE_{zpe} and ΔS are the difference of enthalpy, the zero-point energy and the entropy of each elementary reaction, respectively. Set T to the appropriate temperature in each calculation step. In addition, ΔE_{zpe} is attained through vibration frequency analysis.

Evaluation of nanofiltration performance. The nanofiltration performance was determined using dead-end filtration of various dye solutions (25 ppm). ZnO/rGO and GO membranes were loaded on nylon substrates by a simple vacuum filtration. The thicknesses of the membranes were controlled by the weight of ZnO/rGO nanocomposites (or GO), and the nanosheets loading amount is controlled at 0.54 mg cm^{-2}. Each membrane was analyzed in triplicates under the same conditions. The feed and permeate concentrations were analyzed by ultraviolet-visible (UV-Vis) spectroscopy, which was measured at the maximal absorption wavelength of the five organic dyes.

Filtration characteristics, including water permeability (J, L m^{-2} h^{-1} bar^{-1}) and dye rejection (R, %), were calculated by the following equations:

$$J = \frac{J_W}{P} = \frac{V}{AtP}$$

3

Where V is the volume of permeate (L), A is effective membrane area ($4 \cdot 10^{-4}$ m^2,), t is the permeation time (h), and ΔP is the transmembrane pressure (1 bar).

$$R_{(\%)} = \frac{C_f - C_P}{C_f} 100$$

4

Where C_f and C_p are the concentrations of markers in the permeate and retentate solutions.

Declarations

Acknowledgements

Author Contributions

D.H.L. supervised and conceived the idea and wrote the paper. B.N. supervised the project. W.Y.Z. designed experiments, synthesized samples, carried out nanofiltration performance measurement and wrote the paper. X.H. performed the DFT calculations. F.X. and X.H.M. performed nanofiltration performance measurement. H.Y.Z. performed the illustration of reaction process. M.Q.C. and Y.Y.Z. helped with the modification of the paper.

Competing interests

The authors declare no competing interests.

Materials & Correspondence

Corresponding Author

Donghui Long – East China University of Science and Technology, Shanghai 200237, China; orcid.org/0000-0002-3179-4822; E-mail: longdh@mail.ecust.edu.cn

Bo Niu – East China University of Science and Technology, Shanghai 200237, China; orcid.org/0000-0003-4126-6246; E-mail: niubo@ecust.edu.cn

Authors

Wanyu Zhang – East China University of Science and Technology, Shanghai 200237, China;

Hai Xu – East China University of Science and Technology, Shanghai 200237, China;

Fei Xie – East China University of Science and Technology, Shanghai 200237, China;

Xiaohua Ma – East China University of Science and Technology, Shanghai 200237, China;

Mingqi Chen – East China University of Science and Technology, Shanghai 200237, China;

Hongyu Zhang – East China University of Science and Technology, Shanghai 200237, China;

Yayun Zhang – East China University of Science and Technology, Shanghai 200237, China;

References

1. Al-Rashdi, B.A.M., D.J. Johnson, and N. Hilal, *Removal of heavy metal ions by nanofiltration.* Desalination, 2013. **315**: p. 2–17.

2. Marchetti, P., et al., *Molecular separation with organic solvent nanofiltration: a critical review.* Chemical reviews, 2014. **114**(21): p. 10735–10806.

3. Radjenović, J., et al., *Rejection of pharmaceuticals in nanofiltration and reverse osmosis membrane drinking water treatment.* Water research, 2008. **42**(14): p. 3601–3610.

4. Nath, K., H.K. Dave, and T.M. Patel, *Revisiting the recent applications of nanofiltration in food processing industries: Progress and prognosis.* Trends in Food Science & Technology, 2018. **73**: p. 12–24.

5. Sun, S.P., et al., *Polyamide-imide nanofiltration hollow fiber membranes with elongation-induced nano-pore evolution.* AIChE Journal, 2009. **56**(6): p. 1481–1494.

6. Baker, R.W., *Membrane technology and applications.* 2012: John Wiley & Sons.

7. Cheng, C., S.A. Iyengar, and R. Karnik, *Molecular size-dependent subcontinuum solvent permeation and ultrafast nanofiltration across nanoporous graphene membranes.* Nature Nanotechnology, 2021: p. 1–7.

8. Pandey, R.P., et al., *A fouling-resistant mixed-matrix nanofiltration membrane based on covalently cross-linked Ti3C2TX (MXene)/cellulose acetate.* Journal of Membrane Science, 2020. **607**: p. 118139.

9. Akbari, A., et al., *Large-area graphene-based nanofiltration membranes by shear alignment of discotic nematic liquid crystals of graphene oxide.* Nature communications, 2016. **7**(1): p. 1–12.

10. Zhu, Y., et al., *Graphene and graphene oxide: synthesis, properties, and applications.* Adv Mater, 2010. **22**(35): p. 3906–24.

11. Yang, Y., et al., *Large-area graphene-nanomesh/carbon-nanotube hybrid membranes for ionic and molecular nanofiltration.* Science, 2019. **364**(6445): p. 1057–1062.

12. Yuan, Y., et al., *Enhanced desalination performance of carboxyl functionalized graphene oxide nanofiltration membranes*. Desalination, 2017. **405**: p. 29–39.

13. Dubin, S., et al., *A one-step, solvothermal reduction method for producing reduced graphene oxide dispersions in organic solvents*. ACS nano, 2010. **4**(7): p. 3845–3852.

14. Feldmann, C. and H.O. Jungk, *Polyol-mediated preparation of nanoscale oxide particles*. Angewandte Chemie International Edition, 2001. **40**(2): p. 359–362.

15. Hamilton, C.E., et al., *High-yield organic dispersions of unfunctionalized graphene*. Nano letters, 2009. **9**(10): p. 3460–3462.

16. Han, Y., Z. Xu, and C. Gao, *Ultrathin graphene nanofiltration membrane for water purification*. Advanced Functional Materials, 2013. **23**(29): p. 3693–3700.

17. Huang, K., et al., *A graphene oxide membrane with highly selective molecular separation of aqueous organic solution*. Angewandte Chemie, 2014. **126**(27): p. 7049–7052.

18. Liu, J., et al., *Bioinspired graphene membrane with temperature tunable channels for water gating and molecular separation*. Nature communications, 2017. **8**(1): p. 1–9.

19. Zhang, L., et al., *Fungal Cell Wall-Graphene Oxide Microcomposite Membrane for Organic Solvent Nanofiltration*. Advanced Functional Materials, 2021. **31**(23).

20. Koenig, S.P., et al., *Selective molecular sieving through porous graphene*. Nature nanotechnology, 2012. **7**(11): p. 728–732.

21. Zheng, S., et al., *Correlating interlayer spacing and separation capability of graphene oxide membranes in organic solvents*. ACS nano, 2020. **14**(5): p. 6013–6023.

22. Iakunkov, A. and A.V. Talyzin, *Swelling properties of graphite oxides and graphene oxide multilayered materials*. Nanoscale, 2020. **12**(41): p. 21060–21093.

23. Qi, B., et al., *Strict molecular sieving over electrodeposited 2D-interspacing-narrowed graphene oxide membranes*. Nat Commun, 2017. **8**(1): p. 825.

24. Liu, H., H. Wang, and X. Zhang, *Facile fabrication of freestanding ultrathin reduced graphene oxide membranes for water purification*. Advanced materials, 2015. **27**(2): p. 249–254.

25. Wei, Y., et al., *Declining flux and narrowing nanochannels under wrinkles of compacted graphene oxide nanofiltration membranes*. Carbon, 2016. **108**: p. 568–575.

26. Karachevtsev, V.A., et al., *Structural and spectral transformation of cationic porphyrin TMPyP4 at adsorption on graphene*. Journal of Molecular Structure, 2021: p. 131056.

27. Zhang, W., et al., *Soft Particles Enable Fast and Selective Water Transport through Graphene Oxide Membranes*. Nano Letters, 2020. **20**(10): p. 7327–7332.

28. Dai, L., et al., *Ultrafast Water Transport in Two-Dimensional Channels Enabled by Spherical Polyelectrolyte Brushes with Controllable Flexibility*. Angew Chem Int Ed Engl, 2021.

29. Shao, L., et al., *Tuning the performance of polypyrrole-based solvent-resistant composite nanofiltration membranes by optimizing polymerization conditions and incorporating graphene oxide*. Journal of Membrane Science, 2014. **452**: p. 82–89.

30. Gao, T., et al., *Enhanced stability and separation efficiency of graphene oxide membranes in organic solvent nanofiltration*. Journal of Materials Chemistry A, 2018. **6**(40): p. 19563–19569.

31. Lai, G.S., et al., *Graphene oxide incorporated thin film nanocomposite nanofiltration membrane for enhanced salt removal performance*. Desalination, 2016. **387**: p. 14–24.

32. Aba, N.F.D., et al., *Graphene oxide membranes on ceramic hollow fibers–Microstructural stability and nanofiltration performance*. Journal of Membrane Science, 2015. **484**: p. 87–94.

33. Xue, Y., et al., *Multiscale patterning of graphene oxide and reduced graphene oxide for flexible supercapacitors*. Carbon, 2015. **92**: p. 305–310.

34. Dikin, D.A., et al., *Preparation and characterization of graphene oxide paper*. Nature, 2007. **448**(7152): p. 457–460.

35. Bae, G., et al., *Complementary Dual-Channel Gas Sensor Devices Based on a Role-Allocated ZnO/Graphene Hybrid Heterostructure*. ACS Applied Materials & Interfaces, 2019. **11**(18): p. 16830–16837.

36. Qi, X., et al., *Conjugated-polyelectrolyte-functionalized reduced graphene oxide with excellent solubility and stability in polar solvents*. Small, 2010. **6**(5): p. 663–669.

37. Ma, Q., et al., *Colloidal dispersion of Nb2O5/reduced graphene oxide nanocomposites as functional coating layer for polysulfide shuttle suppression and lithium anode protection of Li-S battery*. J Colloid Interface Sci, 2020. **566**: p. 11–20.

38. Paek, S.-M., E. Yoo, and I. Honma, *Enhanced cyclic performance and lithium storage capacity of SnO2/graphene nanoporous electrodes with three-dimensionally delaminated flexible structure*. Nano letters, 2009. **9**(1): p. 72–75.

39. Wang, Z., et al., *Graphene oxide nanofiltration membranes for desalination under realistic conditions*. Nature Sustainability, 2021. **4**(5): p. 402–408.

40. Shen, J., et al., *Artificial channels for confined mass transport at the sub-nanometre scale*. Nature Reviews Materials, 2021. **6**(4): p. 294–312.

41. Chen, L., et al., *High performance hierarchically nanostructured graphene oxide/covalent organic framework hybrid membranes for stable organic solvent nanofiltration*. Applied Materials Today, 2020. **20**.

42. Kang, H., et al., *Sandwich morphology and superior dye-removal performances for nanofiltration membranes self-assemblied via graphene oxide and carbon nanotubes*. Applied Surface Science, 2018. **428**: p. 990–999.

43. Mehrabi, N., H. Lin, and N. Aich, *Deep eutectic solvent functionalized graphene oxide nanofiltration membranes with superior water permeance and dye desalination performance*. Chemical Engineering Journal, 2021. **412**.

44. Qiu, Z., X. Ji, and C. He, *Fabrication of a loose nanofiltration candidate from Polyacrylonitrile/Graphene oxide hybrid membrane via thermally induced phase separation*. J Hazard Mater, 2018. **360**: p. 122–131.

45. Suriani, A.B., et al., *Incorporation of Electrochemically Exfoliated Graphene Oxide and TiO2 into Polyvinylidene Fluoride-Based Nanofiltration Membrane for Dye Rejection*. Water, Air, & Soil Pollution, 2019. **230**(8).

46. Wang, L., et al., *Layer-by-layer self-assembly of polycation/GO nanofiltration membrane with enhanced stability and fouling resistance*. Separation and Purification Technology, 2016. **160**: p. 123–131.

47. Wang, N., et al., *Self-assembly of graphene oxide and polyelectrolyte complex nanohybrid membranes for nanofiltration and pervaporation*. Chemical Engineering Journal, 2012. **213**: p. 318–329.

48. Wu, Y., et al., *2D Heterostructured Nanofluidic Channels for Enhanced Desalination Performance of Graphene Oxide Membranes*. ACS Nano, 2021. **15**(4): p. 7586–7595.

49. Yang, K., et al., *Graphene Oxide Nanofiltration Membranes Containing Silver Nanoparticles: Tuning Separation Efficiency via Nanoparticle Size*. Nanomaterials (Basel), 2020. **10**(3).

50. Zhang, W.H., et al., *Graphene oxide membranes with stable porous structure for ultrafast water transport*. Nat Nanotechnol, 2021. **16**(3): p. 337–343.

51. Zhong, Y., et al., *Graphene oxide modified membrane for highly efficient wastewater treatment by dynamic combination of nanofiltration and catalysis*. J Hazard Mater, 2020. **397**: p. 122774.

52. Marcano, D.C., et al., *Improved synthesis of graphene oxide*. ACS nano, 2010. **4**(8): p. 4806–4814.
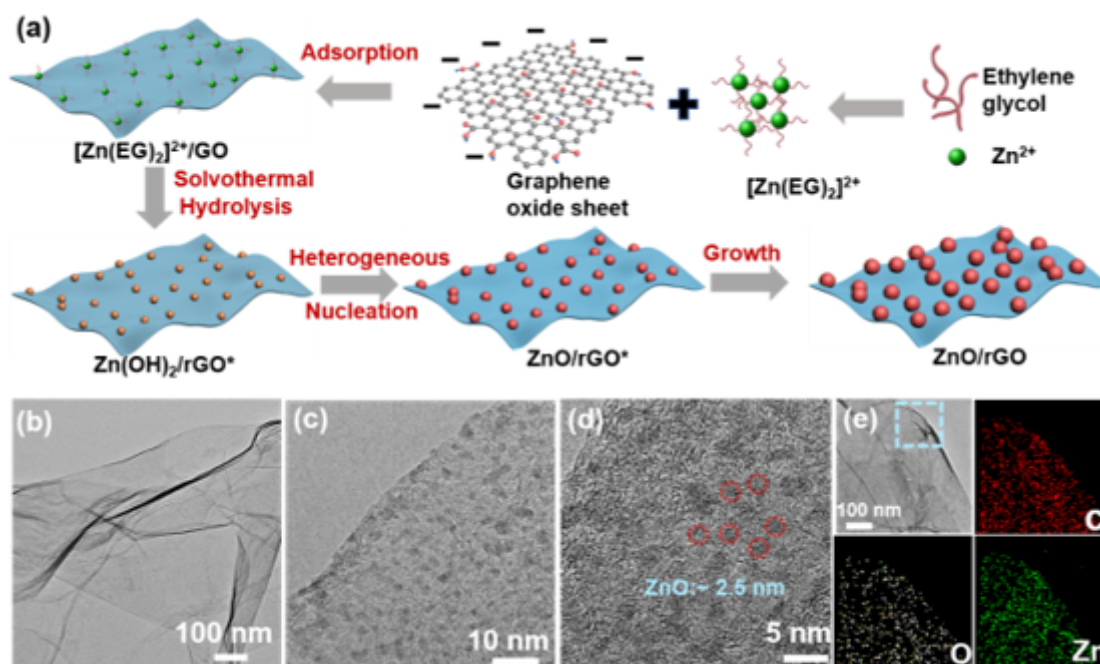
Figures

Figure 1

Synthesis and characterization of ultrafine ZnO/rGO nanocomposites. (a) Schematic illustration of the growth mechanism of ultrafine ZnO/rGO nanocomposites. (b-d) TEM images of ZnO/rGO at different magnifications. (i) TEM elemental mapping images of ZnO/rGO.
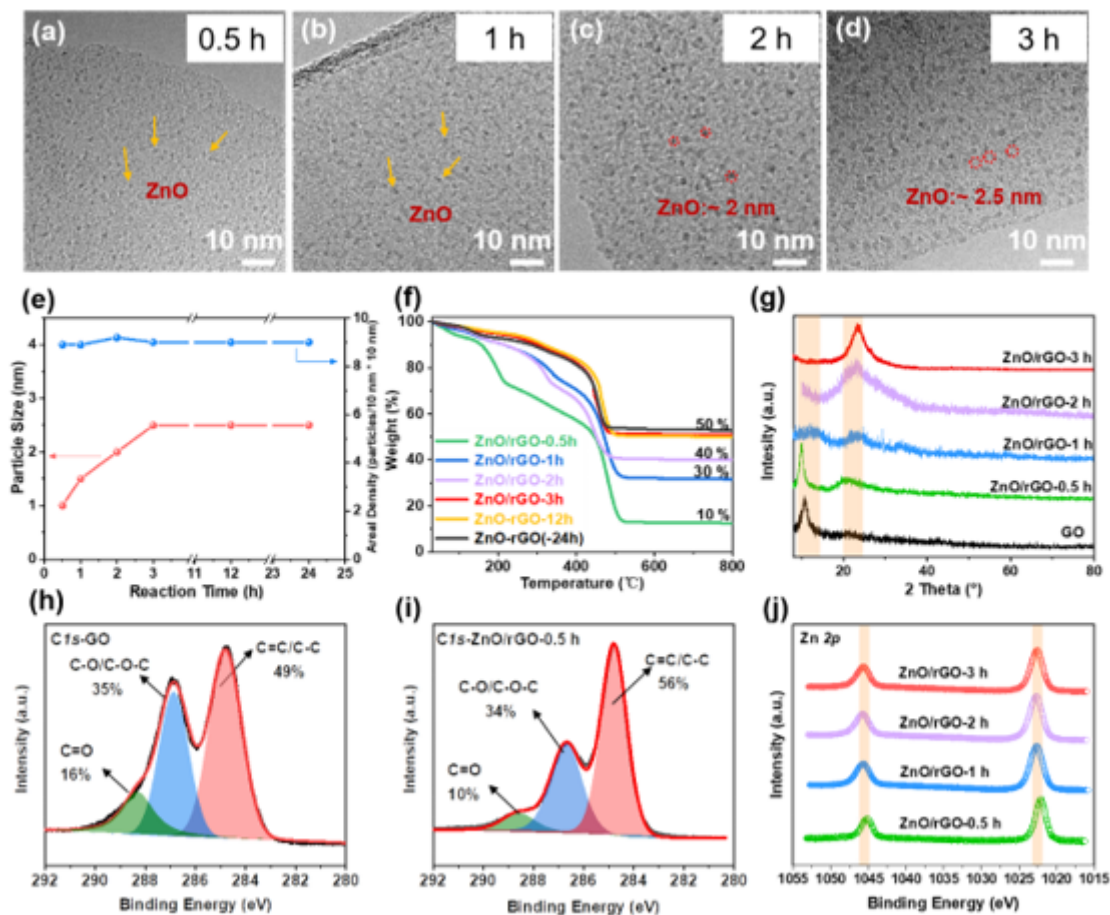

Figure 2

Mechanism study of the formation of ultrafine ZnO nanoparticles on GO surface. TEM images of (a) ZnO/rGO-0.5h, (b) ZnO/rGO-1h, (c) ZnO/rGO-2h and (d) ZnO/rGO-3h. (e) Graph of the average particle size and particle number density over time. (f) TGA curves and (g) XRD spectra of various samples. C1s XPS spectra of (h) GO, (i) ZnO/rGO-0.5 h and (j) Zn 2p XPS spectra of various samples.
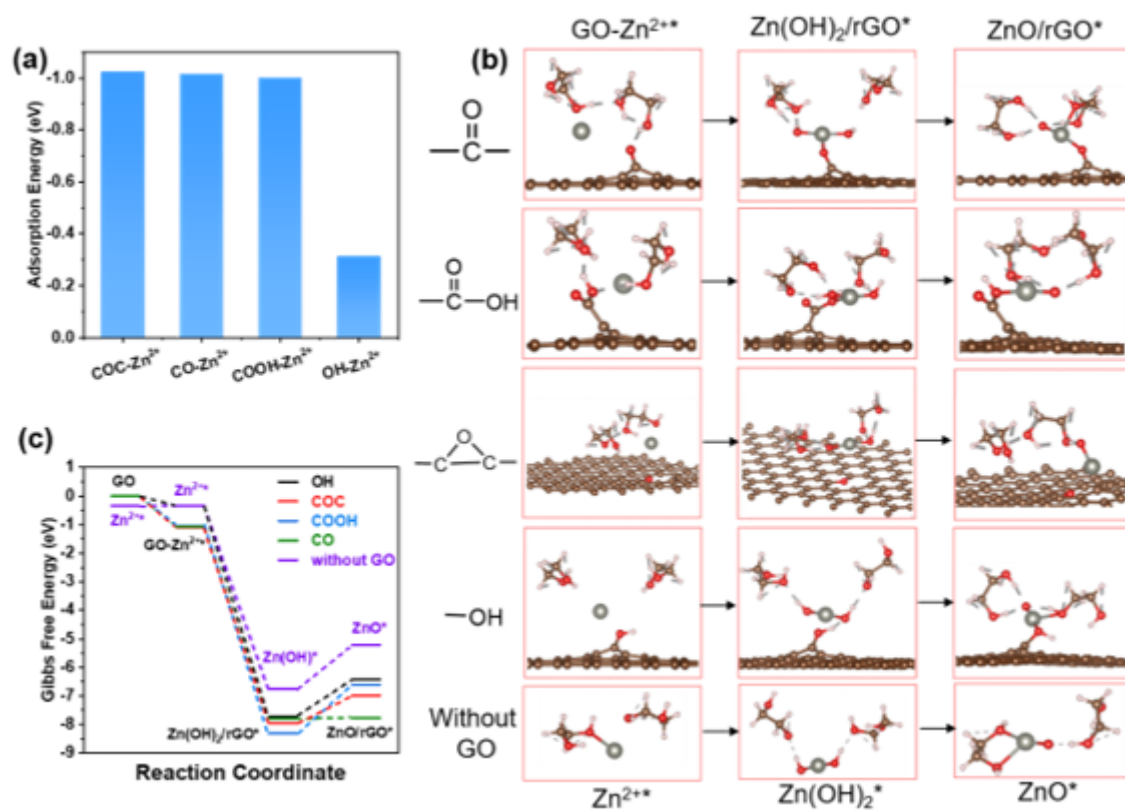
Figure 3

DFT calculations of the formation of ultrafine ZnO nanoparticles on GO surface. (a) Adsorption Energy of Zn2+ on functional groups. (b) The optimized adsorption conformations of intermediate species on GO surface functional groups and in the absence of GO in EG. (c) Energy profiles for the formation of ZnO nanoparticles on GO surface functional groups and in the absence of GO in EG.
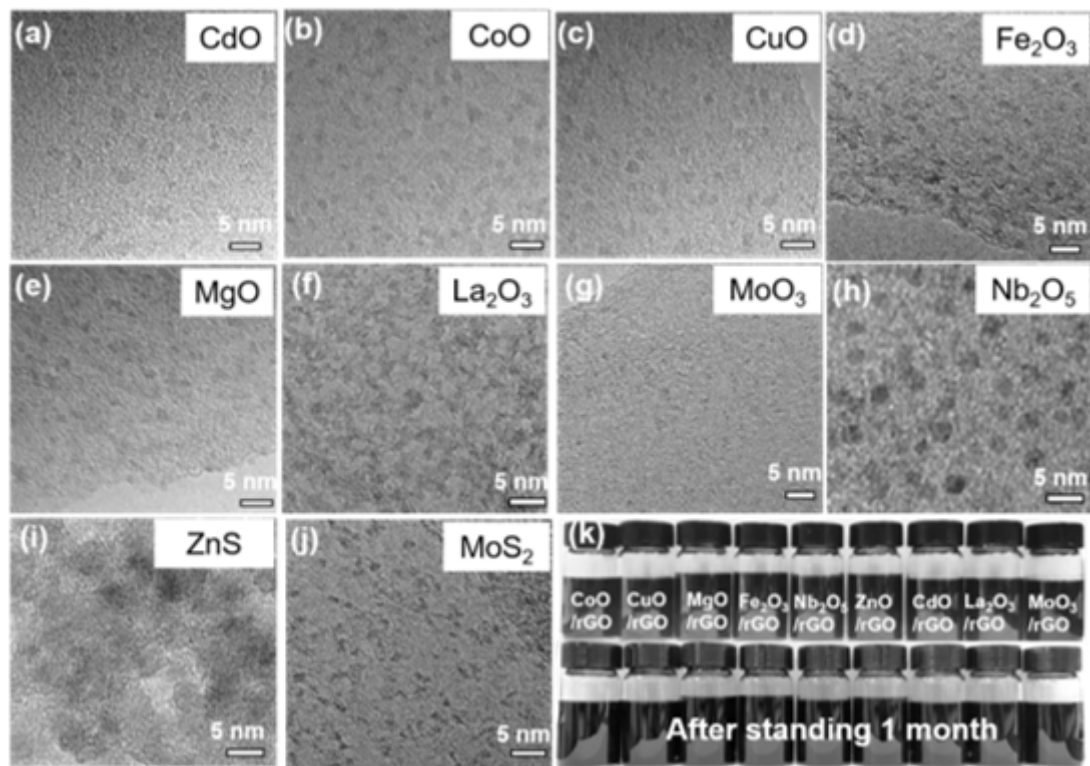
Figure 4

Characterization of other ultrafine metal oxide/rGO nanocomposites. TEM images of (a) CdO/rGO, (b) CoO/rGO, (c) CuO/rGO, (d) Fe2O3/rGO, (e) MgO/rGO, (f) La2O3/rGO, (g) MoO3/rGO, (h) Nb2O5/rGO, (i) ZnS/rGO, and (j) MoS2/rGO nanocomposites, respectively. (k) Colloidal solution of various metal oxide/rGO standing 1 month and without standing.
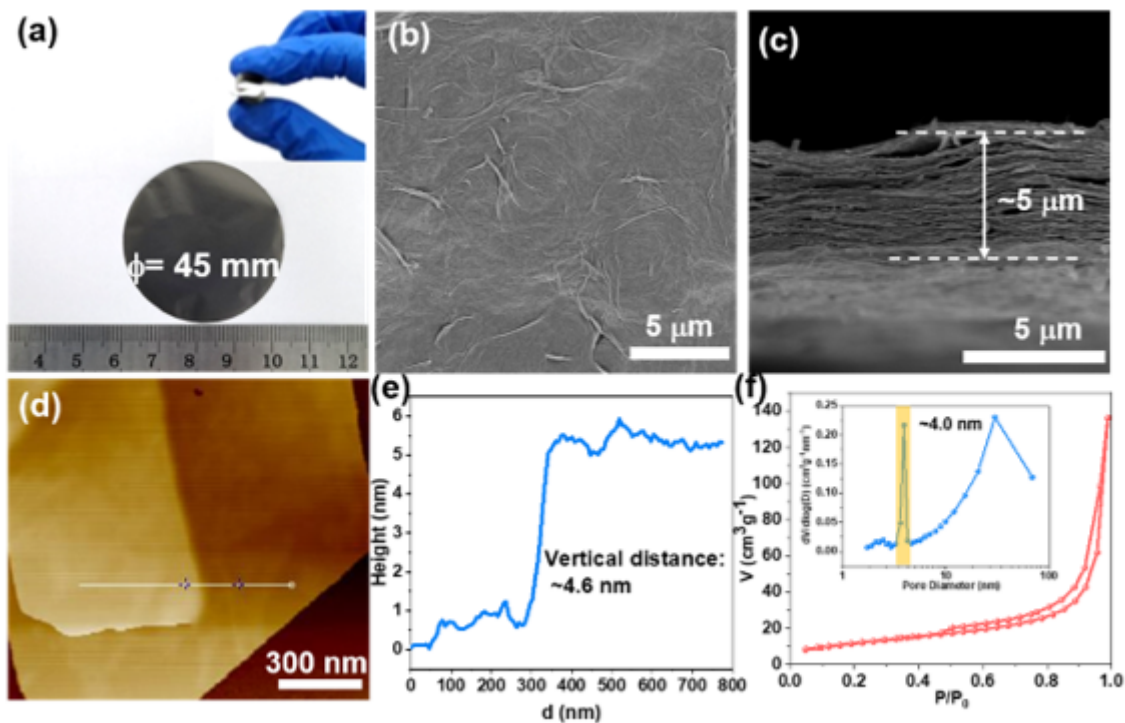
Figure 5

Characterizations of ZnO/rGO membranes. (a) Digital photograph of the ZnO/rGO membranes, (b) top-view SEM image and (c) cross-section SEM images of ZnO/rGO membranes. (d-e) AFM images of ZnO/rGO membranes. (f) N2 adsorption-desorption isotherm and corresponding pore size distribution (inset) of ZnO/rGO membranes.
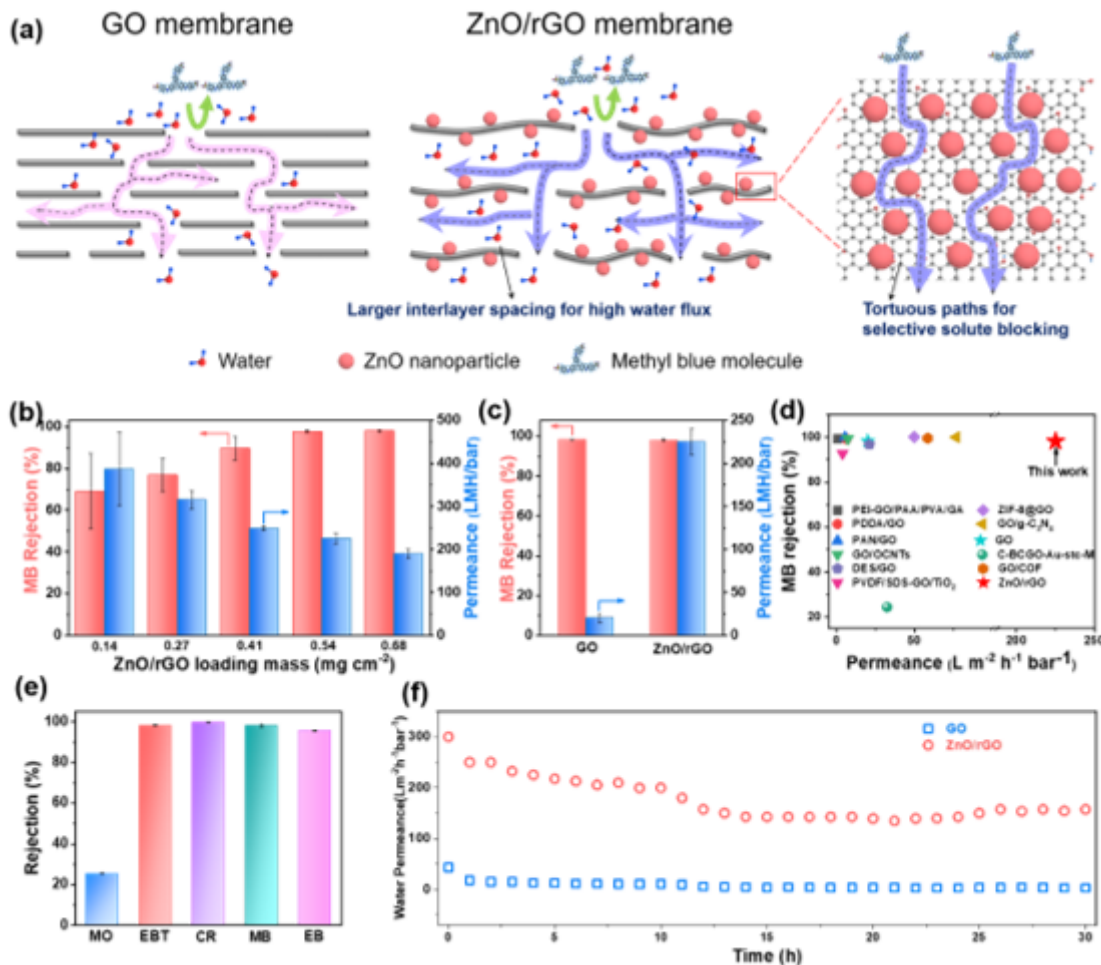

Figure 6

Nanofiltration performance of ZnO/rGO and GO membranes. (a) Schematic illustration of water transport through GO membranes and ZnO/rGO membranes. (b) Water permeance and MB rejection for ZnO/rGO membranes with different thickness. The blue and red arrows represent data corresponding to water permeance and MB rejection, respectively. (c) Water permeance and MB rejection for ZnO/rGO membranes and GO membranes. (d) Comparation of water permeance and MB rejection of reported GO-based membranes. (e) Separation performance of ZnO/rGO for negatively charged molecules of varying molecular weight: Evans Blue (EB, MW=960), Congo Red (CR, MW=696), Chrome Black T (CBT, MW=461) and Methyl Orange (MO, MW=327). (f) Pure water permeance of ZnO/rGO membranes and GO membranes over a 30-h operating period.

Supplementary Files

This is a list of supplementary files associated with this preprint. Click to download.

- SupplementaryInformation1.docx